

# Verification of independent quantum devices

C. Greganti,<sup>1,2,\*</sup> T. F. Demarie,<sup>3,4,5,\*</sup> M. Ringbauer,<sup>6</sup> J. A. Jones,<sup>7</sup> V. Saggio,<sup>1</sup> I. A. Calafell,<sup>1</sup> L. A. Rozema,<sup>1</sup> A. Erhard,<sup>6</sup> M. Meth,<sup>6</sup> L. Postler,<sup>6</sup> R. Stricker,<sup>6</sup> P. Schindler,<sup>6</sup> R. Blatt,<sup>6,8</sup> T. Monz,<sup>6,9</sup> P. Walther,<sup>1</sup> and J. F. Fitzsimons<sup>4,5,10</sup>

<sup>1</sup>Vienna Center for Quantum Science and Technology (VCQ), Faculty of Physics,  
University of Vienna, Boltzmanngasse 5, Vienna A-1090, Austria

<sup>2</sup>VitreaLab GmbH, Boltzmanngasse 5, A-1090 Vienna, Austria

<sup>3</sup>Entropica Labs, 32 Carpenter Street, Singapore 059911

<sup>4</sup>Centre for Quantum Technologies, National University of Singapore, 3 Science Drive 2, Singapore 117543

<sup>5</sup>Singapore University of Technology and Design, 8 Somapah Road, Singapore 487372

<sup>6</sup>Institut für Experimentalphysik, Universität Innsbruck, Technikerstrasse 25, A-6020 Innsbruck, Austria

<sup>7</sup>Clarendon Laboratory, Department of Physics, University of Oxford, Parks Road, Oxford OX1 3PU, U.K.

<sup>8</sup>Institut für Quantenoptik und Quanteninformation, Österreichische Akademie  
der Wissenschaften, Otto-Hittmair-Platz 1, A-6020 Innsbruck, Austria

<sup>9</sup>Alpine Quantum Technologies GmbH, 6020 Innsbruck, Austria

<sup>10</sup>Horizon Quantum Computing, 79 Ayer Rajah Crescent, #03-01 BASH, Singapore 139955<sup>†</sup>

Quantum computers are on the brink of surpassing the capabilities of even the most powerful classical computers. This naturally raises the question of how one can trust the results of a quantum computer when they cannot be compared to classical simulation. Here we present a scalable verification technique that exploits the principles of measurement-based quantum computing to link quantum circuits of different input size, depth, and structure. Our approach enables consistency checks of quantum computations within a device, as well as between independent devices. We showcase our protocol by applying it to five state-of-the-art quantum processors, based on four distinct physical architectures: nuclear magnetic resonance, superconducting circuits, trapped ions, and photonics, with up to 6 qubits and more than 200 distinct circuits.

Quantum computers represent a fundamental shift in the way we think about computation. By harnessing quantum interference effects between different possible branches of a computation, quantum processors have the potential to drastically outperform conventional computers for a range of tasks [1–6]. Potential applications of quantum computing range from cryptanalysis to the simulation of physical systems and even to machine learning. Extraordinary experimental efforts in recent years have enabled demonstrations of the technology’s potential in a growing number of physical systems [7–10]. For certain simulation tasks, these devices are already starting to push the limits of classical supercomputers [11, 12], and it is foreseeable that the next generation of digital quantum processors will outperform their classical counterparts.

Despite the potential power of quantum computers, building reliable quantum processors remains a challenge. Environmental interactions introduce noise into the computation, yielding potentially unreliable results for complex computations. This naturally leads to the question of whether we can trust the output of a quantum computation, and, more concretely, whether we can certify the output of a computation as correct. One possibility might be to repeat a quantum computation multiple times, or even on different devices. However, this merely establishes that the devices operate in a reproducible fashion, but is insensitive to systematic errors and thus cannot reliably verify the computation. Significant work has gone into the development of cryptographically secure verification protocols [13–20], with one such technique having been experimentally demonstrated [21]. However, existing provably secure verification techniques require either quantum communication [13–16] or shared entanglement between devices [17–20], making them challenging to imple-

ment in existing systems where quantum processors are typically unable to exchange quantum states with one another. A promising technique has recently been proposed to allow verification of a single isolated processor based on computational hardness assumptions [22], however this would require an extremely sophisticated processor to implement, due to large key sizes.

Here we address the question of whether one device can be used to efficiently check another device, without relying on quantum communication or entanglement between devices. We introduce a cross-check procedure that is inherently agnostic to the underlying hardware, sensitive to systematic errors in the implementation, and applicable to any digital quantum computation. The protocol is built on the framework of measurement-based quantum computing (MBQC) [23, 24], which has proven a powerful tool for blind and verifiable computing protocols [25]. By exploiting the intrinsic symmetries of quantum circuits when mapped to a measurement-based computation, our approach allows us to quantitatively compare the outputs of quantum circuits with different size and structure, performed on independent physical devices in any architecture, thus building a high level of trust in the results of the computation. We demonstrate our protocol by running 200 circuits on five state-of-the-art quantum processors, using four primary technologies for digital quantum computation: 1) nuclear magnetic resonance (NMR), 2) superconducting circuits, 3) trapped ions, and 4) photonics, see Fig. 1.

In order to verify the correctness of a quantum computation we make use of independent runs of several different yet related sampling problems, obtained from a measurement-based implementation of the computation. In contrast to the standard circuit model of quantum computing, where a unitary

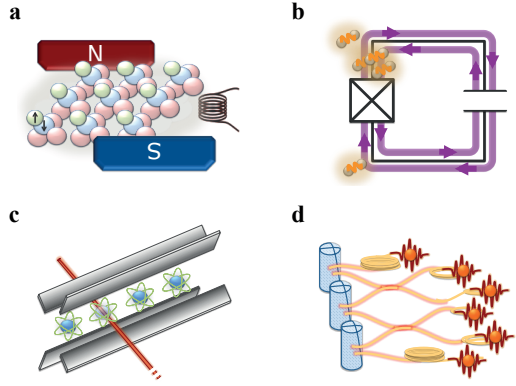


**FIG. 1. A cartoon representation of the quantum processing architectures used.** **a)** An NMR device at the University of Oxford [7]; **b)** superconducting circuits at IBM [26] and Rigetti Computing [27]; **c)** a trapped-ion quantum processor at the University of Innsbruck [8]; and **d)** a photonic quantum processor at the University of Vienna [28].

operation is described by a sequence of gates applied to a reference input, for instance  $|0\rangle^{\otimes N}$ , in MBQC a computation is realized as a sequence of single-qubit measurements performed on highly entangled multi-qubit states. These states are also known as *graph states* for their one-to-one correspondence with simple graphs  $\mathcal{G} = \{\mathcal{V}, \mathcal{E}\}$ , represented by a set of vertices  $\mathcal{V}$ , corresponding to single qubits initialized in the state  $|+\rangle = (|0\rangle + |1\rangle)/\sqrt{2}$ , and a set of edges  $\mathcal{E}$ , corresponding to pairwise controlled-Z entangling gates applied to the respective vertices, see Supplementary Material for details. The MBQC model is computationally equivalent to the circuit model for appropriate families of graphs [23], even when measurements are restricted to the XY-plane of the Bloch sphere [29], as considered here.

One way to visualize a quantum computation as an MBQC pattern is to identify subsets of vertices on the graph as input and output sets: the input set represents the initial state of the computation, and the output set will contain the final state once all other qubits have been measured.

A deterministic computation is implemented by sequentially measuring the non-output (also called *operational*) qubits and applying outcome-dependent corrections to the unmeasured neighbouring qubits. By convention, a measurement outcome of zero requires no correction, whereas a measurement outcome of one requires a correction. For a given choice of input and output sets, a unique set of paths can be identified between each qubit in the input set and a corresponding qubit in the output set. These paths dictate how the corrections, i.e. the updating of measurement angles, should be applied, giving rise to the notions of *flow* [30] and *generalized flow* (*g-flow*) [31]. These flow structures thus specify the possible circuits over a graph by determining the appropriate corrections for non-zero measurement outcomes and their order.

The key insight that we make use of is that, although MBQC performs a deterministic computation between a specific choice of input and output sets, there are always multiple such choices for a given graph. Consequently, there are multiple possible information flows, a concept known as *flow ambiguity* [32]. These alternate flows give rise to computations that require different outcome-dependent corrections. The left side of Figure 2 shows an example of two different flows on an H-shaped 6-qubit graph, with the associated circuits shown on the right. In MBQC, flow-dependent corrections are uniformly random and effectively insert random Z-gates into a fixed circuit determined by the graph and the choice of output set. Thus an MBQC implementing a deterministic computation can also be seen as providing the outcomes of a random set of other computations, each related to a unique computation in the circuit model. Our strategy will be to choose several such related computations, and run each independently, on a distinct physical device, and compare the results. As these computations can have different numbers of logical qubits, this approach provides a natural means for testing devices of differing complexity against one another.

Formally, we now consider an  $n$ -qubit graph state  $|\mathcal{G}\rangle$ , where each qubit is subject to a projective measurement, given by  $P_\theta = \frac{1}{\sqrt{2}}(|0\rangle + e^{-i\theta}|1\rangle)$ , at an angle  $\theta$  in the XY-plane of the Bloch-sphere. The probability of a particular measurement string of zero and one outcomes,  $m = m_1 \dots m_n$ ,

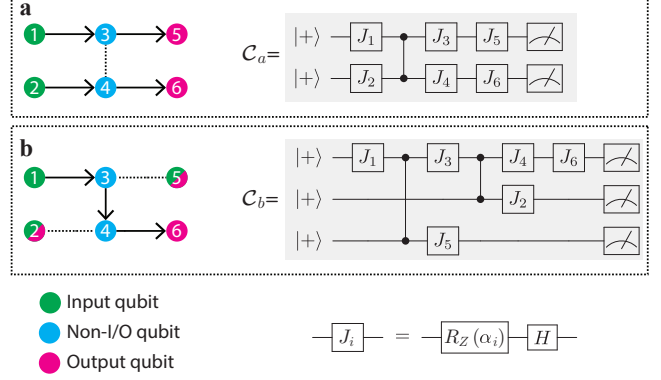


**FIG. 2. Schematic representation of equivalent computations in MBQC (left) and in the circuit model (right).** The MBQC graph state is a six-qubit H-shaped cluster state with 2 different g-flows, consisting of a) 4 and b) 3 operational qubits. The direction of the flow is indicated by the arrows on the graph, with edges not involved in flow shown as a dashed line. The qubits are measured according to the order of the labelling numbers. In (a) the input state of the circuit  $C_a$  is  $|++\rangle$ , associated with qubits 1 and 2 of the cluster state, whereas in (b) the input state of the circuit  $C_b$  is  $|+++ \rangle$ , associated with qubits 1, 2, and 5 of the cluster state. Note that the quantum circuits on the right correspond to the same MBQC graph state on the left, albeit with a different flow. The basic gate  $\hat{J}(\alpha_i) = \hat{H}\hat{R}_z(\alpha_i)$  (for brevity  $\hat{J}_i$  with  $i = (1, \dots, 6)$ ) can be decomposed into a Hadamard gate  $\hat{H}$  and a rotation  $\hat{R}_z(\alpha)$  around the z-axis of the Bloch sphere, see Supplementary Material for details.

is then given by  $p_{\alpha,m} = |(\bigotimes_{i=1}^n P_{\alpha_i+m_i\pi})|\mathcal{G}\rangle|^2$ , where  $\alpha = \{\alpha_1 \dots \alpha_n\}$  are the measurement angles for qubits 1 to  $n$ . Importantly, for an MBQC with  $n_O$  output vertices, all measurement outcomes over non-output qubits occur with equal probability of  $2^{-(n-n_O)}$  [33]. Hence there is no bias, and using the substitution  $\alpha'_i = \alpha_i + m_i\pi$ , we have  $p_{\alpha,m} = p_{\alpha',0}$  and can, without loss of generality, focus on the measurement string with all zeros where no flow-dependent corrections are necessary. Consequently, there is no preferred choice of output set, and hence the outcome of many different, but related computations can be obtained from  $p_{\alpha',0}$  or equivalently from  $p_{\alpha,m}$ .

We can use this to generate correlated sampling problems by converting a given MBQC with angles  $\alpha'$  into the circuit model for different choices of the output set (which also determines the input set and uniquely identifies the computation). This is illustrated in Fig. 2 on the example of a 6-qubit H-shaped cluster state, from which we obtain circuit  $\mathcal{C}_a$  with  $n_O = 2$  and circuit  $\mathcal{C}_b$  with  $n_O = 3$ . As an example, let us consider the circuit  $\mathcal{C}_a$ . Since all measurement outcomes over non-output qubits occur with probability  $2^{-(n-n_O)}$ , that is  $2^{-4}$  in the considered case, the probability  $p_{\alpha',0_{\mathcal{C}_a}}$  of obtaining a zero outcome when measuring all the 6 qubits is therefore given by  $p_{\alpha',0_{\mathcal{C}_a}} = 2^{-4}\Pr(0,0)_{\mathcal{C}_a}$ , where  $\Pr(0,0)_{\mathcal{C}_a}$  is the probability of obtaining zero outcomes when measuring only the 2 output qubits. Analogously, we obtain  $p_{\alpha',0_{\mathcal{C}_b}} = 2^{-3}\Pr(0,0,0)_{\mathcal{C}_b}$  for the circuit  $\mathcal{C}_b$ . The value of the probabilities  $\Pr(0,0)_{\mathcal{C}_a}$  and  $\Pr(0,0,0)_{\mathcal{C}_b}$  depend on the chosen measurement angles  $\{\alpha_i\}_{i=1}^6$ . Since both circuits  $\mathcal{C}_a$  and  $\mathcal{C}_b$  are encoded into the same graph, the output probabilities for all the outcomes with fixed values are identical for the two circuits, i.e.  $p_{\alpha',0_{\mathcal{C}_a}} = p_{\alpha',0_{\mathcal{C}_b}}$ . This fact allows us to find that  $\Pr(0,0)_{\mathcal{C}_a} = 2\Pr(0,0,0)_{\mathcal{C}_b}$ , thus correlating the outcome probabilities of the two circuits. Similarly, we can write this relation for different combinations of outcome probabilities, thus finding that  $\Pr(0,1)_{\mathcal{C}_a} = 2\Pr(1,0,0)_{\mathcal{C}_b}$ ,  $\Pr(1,0)_{\mathcal{C}_a} = 2\Pr(0,0,1)_{\mathcal{C}_b}$ , and  $\Pr(1,1)_{\mathcal{C}_a} = 2\Pr(1,0,1)_{\mathcal{C}_b}$ .

This is a crucial insight that establishes a connection between the outcome probabilities from two quantum circuits with different width, depth, and structure, but with correlated angles for the single-qubit gates. Implementing these circuits ( $\mathcal{C}_a$  and  $\mathcal{C}_b$  in the case of the current experiments) on a single device provides a means for self-verification of the device, while implementing them on different devices provides a pathway to cross-validate the two devices. More generally, all output strings over shared output qubits can be related across circuits, as we describe in detail in the Supplementary Material. Moreover, one can randomize the output strings by adding a random multiple of  $\pi$  to the measurement angles for the qubits in the output set. This would allow us to create two distinct, but related circuits such that the probability of obtaining particular (non-zero) strings as outputs is correlated.

In order to formally turn this approach into a test of consistency between quantum devices, we now consider two quantum processors implementing computations derived from the same MBQC but with different output sets. For output sets

of sizes  $n_{O_1}$  and  $n_{O_2}$ , with  $n_c$  qubits that are in both output sets, and fixing all outcomes corresponding to qubits, which are not in the output set of either computation to 0, we are left with  $n_v = n_{O_1} + n_{O_2} - n_c$  variable bits and thus  $2^{n_v}$  different measurement strings  $m$  to consider. Denoting the vector of probabilities of each  $m$  obtained by performing the quantum circuit  $\mathcal{C}_j$  on the  $j^{\text{th}}$  device (normalized as above) by  $\mathbf{p}_j$ , we can compare the probability distributions of different devices by computing the squared  $\ell^2$ -distance  $\|\mathbf{p}_1 - \mathbf{p}_2\|^2 = \mathbf{p}_1 \cdot \mathbf{p}_1 - 2\mathbf{p}_1 \cdot \mathbf{p}_2 + \mathbf{p}_2 \cdot \mathbf{p}_2$ . Here,  $\mathbf{p}_j \cdot \mathbf{p}_j$  is the probability of obtaining the same result when running the computation on the  $j^{\text{th}}$  device twice. This probability can be estimated from the minimum number of runs required to obtain a collision among output strings (i.e. obtain the same string twice) which is at most  $O(2^{n_{O_j}/2})$ , independent of the probability distribution, due to a generalization of the birthday paradox [34]. The term  $\mathbf{p}_1 \cdot \mathbf{p}_2$  can be estimated in a similar way by randomly fixing the remaining variable non-output qubits in each computation and estimating the number of runs to obtain a collision between the sets, which is at most  $O(2^{(n_{O_1}+n_{O_2}-n_c)/2})$ . The precise scaling of our method thus depends on the problem at hand. However, when there is a significant number of output qubits in common between the instances ( $n_c \sim n_{O_1}, n_{O_2}$ ), or where the output distribution for either computation is far from uniform ( $\max \mathbf{p}_j \gg 2^{-n_{O_j}}$ ), the quantity  $\|\mathbf{p}_1 - \mathbf{p}_2\|^2$  provides a measure of similarity between the outputs of the corresponding quantum computations, which can be estimated with exponentially fewer resources than conventional classical simulation techniques, which scale at least as  $2^{n_{O_j}}$ . Moreover, we can estimate the squared  $\ell^2$ -distance for circuits of different size and depths performed on a same device for self-verification of a single device.

We experimentally perform correlated 2- and 3-qubit circuits with different depth on five independent small-scale state-of-the-art quantum processors, covering four of the major quantum computing architectures (see Fig. 1): an NMR device [7] at the University of Oxford, simulating 2-qubit computations; a photonic quantum device [28] at the University of Vienna, based on a 6-qubit cluster state; a cloud-accessible superconducting system from IBM [26], performing 3-, 4-, and 5-qubit computations; a cloud-accessible superconducting processor from Rigetti [27] running 3-qubit computations; and a trapped-ion quantum processor [8] at the University of Innsbruck, performing 2- and 3-qubit computations.

Using these devices, we experimentally implemented correlated sampling instances for the six-qubit H-shaped graph shown in Fig. 2 by generating  $\sim 200$  random sets of angles  $\{\alpha_i\}_{i=1}^6$ , with  $\alpha_i \in \{0, \pi/4, \pi/2, 3\pi/4, \pi, 5\pi/4, 3\pi/2, 7\pi/4\}$ . We then ran 2-qubit circuits of type  $\mathcal{C}_a$  on the Oxford and Innsbruck device, 3-qubit circuits of type  $\mathcal{C}_b$  on the IBM and Rigetti processor and the 6-qubit H-shaped MBQC on the Vienna apparatus. After taking into account the known equivalences and required corrections from non-zero outcomes in the underlying MBQC, we analyze the correlations in the output

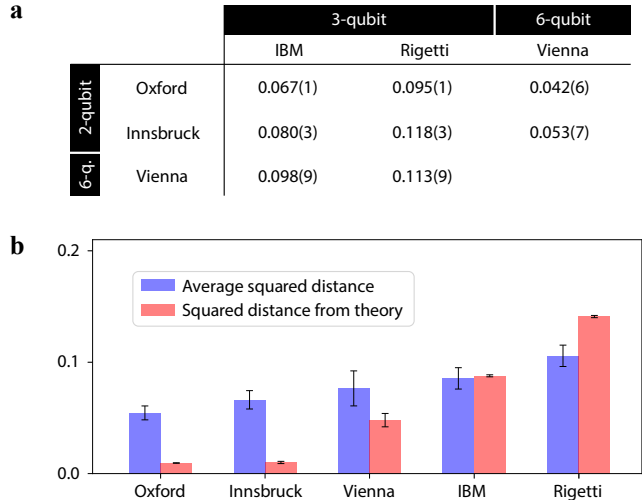


**FIG. 3. Experimental comparison of quantum devices.** a) Experimental distances between two independent devices, where squared  $\ell^2$ -distances are estimated between pairs of independent devices. Each distance is averaged over 34 instances per device. The row contains the devices performing a 2-qubit computation within the circuit model, which are paired to the devices listed in the column of the table implementing the 3-qubit circuits within either the circuit or MBQC model. Only circuits performed using different numbers of physical qubits are compared, so that the circuits correspond to fundamentally different sampling problems. Uncertainties in parenthesis correspond to one standard deviation of statistical noise. b) Value of squared distance per quantum device. For each quantum device the experimental average of the different pair-wise squared  $\ell^2$ -distances in (a) are shown, along side the single-device squared  $\ell^2$ -distance from theory. These quantities are not expected to coincide. However, as can be seen from the figure, arranging devices according to either metric yields the same order in our experiments. Averages are taken over squared  $\ell^2$ -distance between each device and all other devices in order to avoid bias.

strings obtained from the different systems for 34 correlated instances that were implemented on all devices. Crucially, rather than comparing the output strings to some “ideal theory” (e.g. from simulations), which would not be possible for future devices, we compare pairs of correlated instances from different devices.

The key results of these comparisons are summarized in Fig. 3a, estimating the value of the squared  $\ell^2$ -distance for each pair of systems performing different computations in size and depth. A value close to 0 indicates reliable computations, whereas any systematic error or statistical noise will lead to a larger value. In performing these estimates we will scale results by an integer power of two to be directly comparable to the case where  $n_O = 2$ . For example, comparing an ideal to a fully depolarized circuit for the instances considered in our experiments would return a value of  $\sim 0.428$ . Of course, the noise in real experiments is much more complicated and the exact dependence of the squared  $\ell_2$ -distance on such physical noise models remains an interesting question for future research. In order to give some insight into these distances, cor-

relation plots between projectors implemented on all pairs of systems computing different size and depth circuits, are given in Fig. 4. In Fig. 3b we show the squared  $\ell^2$ -distance for each device, averaged over all other devices, and the squared  $\ell^2$ -distance per device in comparison with the ideal theoretical data (in this case still available from classical simulation due to the low number of qubits involved, see Fig. 5 for graphical correlation plots). The averages are taken over all devices, rather than just the comparisons shown in Fig. 3a, in order to avoid biasing the results. In this case the theory results show the accuracy of the individual device, which cannot be extracted from the pairwise comparisons. When more than two devices are considered, however, the average squared distances can be used to infer an approximate ordering of devices in terms of comparison with theory. As can be seen from Fig. 3b, the ordering of devices is the same independent of whether they are sorted by average squared distance or by squared distance from theory. Circuits of larger depths and input size have also been performed on the Oxford, IBM, and Innsbruck systems and are shown in the Supplementary Material.

Besides cross-check verification between dissimilar quantum devices, our method also provides an intriguing pathway towards self-verification of a single device. Using the Innsbruck trapped-ion system, we implemented correlated instances of the 2- and 3-qubit circuits  $C_a$  and  $C_b$  of Fig. 2, and estimate  $\|\mathbf{p}_{C_a} - \mathbf{p}_{C_b}\|^2 = 0.033(1)$ . This result indicates good (relative to the results in Fig. 4a) agreement between the two circuits, which is confirmed by the correlation plot in Fig. 6 and demonstrates that our method can be used for independent verification of a single quantum processor.

As quantum processors start to surpass their classical counterparts, verification by direct comparison to theory will no longer be an option. The technique we present here provides a feasible alternative by validating quantum devices against each other. While not providing a complete toolkit for characterization of individual quantum processors, our method takes a crucial step away from the dependence on classical methods. By sampling from different physical devices implementing circuits that differ in the number of qubits, depth and structure, our method is robust against systematic, as well as statistical errors. By implementing these dissimilar circuits on a single device, our method also provides an avenue towards internal self-verification of single quantum devices.

A particularly intriguing feature of our approach is the way in which it allows us to compare devices using radically different implementations. Recently, a detailed comparison of a trapped ion system and a superconducting processor highlighted the advantages of each system for certain, identical problems [35], concluding that each processor was well suited to different tasks. In this work we overcome the heterogeneity of quantum physical systems, introducing a verification model which links computational circuits with different sizes and depths, and consequently runnable on the many types of quantum computer. The building block of our cross-check scheme is represented by measurement-based quantum computation,

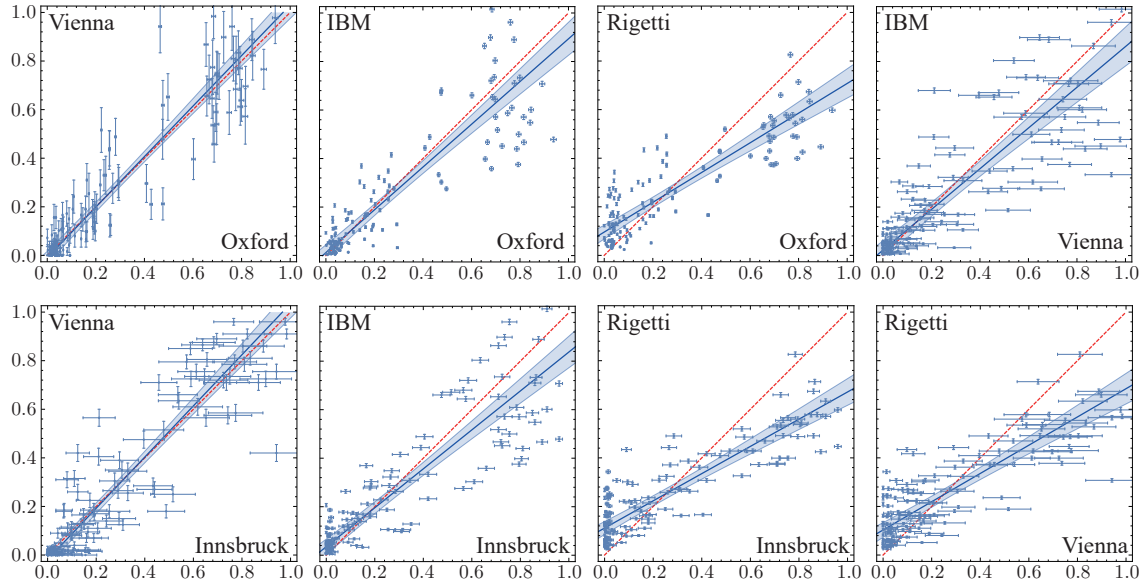


**FIG. 4. Experimental comparison between outputs of computations for pairs of different devices.** Scatterplots of rescaled outcome probabilities for all pairs of different devices implementing different-size circuits. For each dataset containing 136 samples (34 circuits and 4 outcome combinations each), we performed linear total least-squares regression (solid blue line) to quantify the deviation from the ideal correlation (red dashed line), yielding regression slopes with 1-sigma uncertainties of (top, left to right) 1.04(2), 0.88(3), 0.61(2), 0.84(3), (bottom, left to right) 1.05(2), 0.80(3), 0.56(2), and 0.58(2), respectively. Experimental error bars correspond to 1-sigma statistical uncertainty and the blue shaded bands represent 3-sigma mean prediction intervals for the regression.

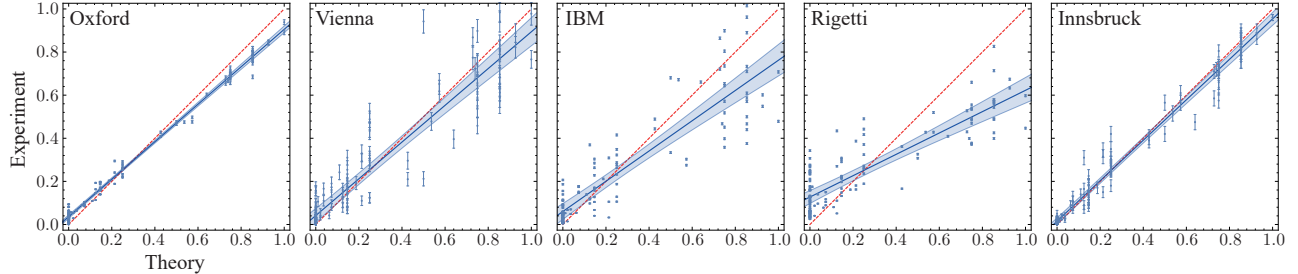


**FIG. 5. Comparison between experimental outcome probabilities and theoretical expected values per single device.** From left to right: Oxford, Vienna, IBM, Rigetti, Innsbruck. For each data set we performed linear least-squares regression (blue line) to quantify the deviation from the ideal correlation (red dashed line), yielding regression slopes with 1-sigma uncertainties of 0.869(6), 0.85(3), 0.70(3), 0.50(2), and 0.94(1), respectively. Experimental error bars correspond to 1-sigma statistical uncertainty and the blue shaded bands represent 3-sigma mean prediction intervals for the regression.

which has been proven to be already essential for quantum computation security [36], quantum error correction [37], as well as quantum simulation [38]. This will prove useful in providing consistent benchmarks across the increasingly diverse range of quantum processors.

**Acknowledgements** We gratefully acknowledge support by the Austrian Science Fund (FWF), through the SFB FoQuS (FWF Project No. F40) and SFB BeyondC (FWF Project No. F71). We also acknowledge funding from the EU H2020-FETFLAG-2018-03 under Grant Agreement no. 820495, and by the U.S. Army Research Office through grant W911NF-14-1-0103. MR acknowledges funding from the

European Union’s Horizon 2020 research and innovation programme under the Marie Skłodowska-Curie grant agreement No 801110 and the Austrian Federal Ministry of Education, Science and Research (BMBWF). PW acknowledges support from the research platform TURIS, the Austrian Science Fund (FWF) through the Doctoral Programme CoQuS (no. W1210-4), BeyondC (F71) and NaMuG (P30067-N36), the United States Air Force Office of Scientific Research via QAT4SECOMP (FA2386-17-1-4011), the European Commission via High dimensional quantum Photonic Platform projects (HiPhOP) (no. 731473) and Red Bull GmbH. JFF acknowledges support from Singapore’s Ministry of Educa-

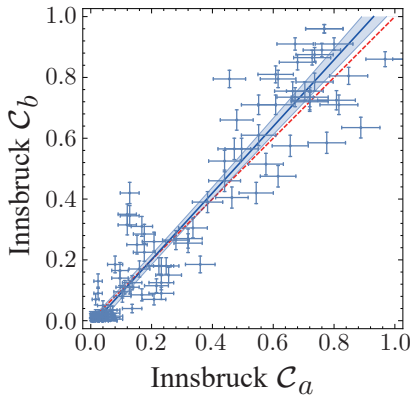


**FIG. 6. Comparison between experimental outcome probabilities for the circuits  $C_a$  and  $C_b$  on the Innsbruck device.** Linear total least-squares regression (solid blue line) yields a regression slope of 1.09(2) compared to the ideal value of 1 (dashed red line). Experimental error bars correspond to 1-sigma statistical uncertainty and the blue shaded bands represent 3-sigma mean prediction intervals for the regression.

tion, National Research Foundation (ANR-NRF Grant No. NRF2017-NRF-ANR004), and the U.S. Air Force Office of Scientific Research (AOARD Grant No. FA2386-18-1-4003).

**Author Contributions** JFF and TFD conceived the project and derived the theory results. CG, VS, IAC, and LAR performed the photonic experiments; MR, AE, MM, LP, RS, PS, and TM performed the trapped ion experiments; JAJ performed the NMR experiments; TFD programmed the superconducting experiments. CG, TFD and MR analyzed the data. RB, TM, PW, and JFF supervised the project. All authors contributed to writing the manuscript.

\* These authors contributed equally to this work.

† [joe@horizonquantum.com](mailto:joe@horizonquantum.com)

- [1] Bernstein, E. & Vazirani, U. Quantum complexity theory. *SIAM J. Comput.* **26**, 1411–1473 (1997).
- [2] Grover, L. K. Quantum Mechanics helps in searching for a needle in a haystack. *Phys. Rev. Lett.* **79**, 325 (1997).
- [3] Simon, D. R. On the Power of Quantum Computation. *SIAM J. Comp.* **26**, 1474–1483 (1997).
- [4] Shor, P. W. Polynomial-Time Algorithms for Prime Factorization and Discrete Logarithms on a Quantum Computer. *SIAM Rev.* **41**, 303–332 (1999).
- [5] Nielsen, M. & Chuang, I. *Quantum Computation and Quantum Information* (Cambridge University Press, 2000).
- [6] Harrow, A. W. & Montanaro, A. Quantum computational supremacy. *Nature* **549**, 203–209 (2017).
- [7] Jones, J. A. Quantum computing with NMR. *Prog. Nucl. Magn. Reson. Spectrosc.* 91–120 (2011).
- [8] Schindler, P. *et al.* A quantum information processor with trapped ions. *New J. Phys.* **15**, 123012 (2013).
- [9] Barz, S. *et al.* A two-qubit photonic quantum processor and its application to solving systems of linear equations. *Sci. Rep.* **4**,

- 6115 (2015).
- [10] Devoret, M. H. & Schoelkopf, R. J. Superconducting Circuits for Quantum Information: An Outlook. *Science* **339**, 1169–1174 (2013).
- [11] Trotzky, S. *et al.* Probing the relaxation towards equilibrium in an isolated strongly correlated one-dimensional Bose gas. *Nat. Phys.* **8**, 325–330 (2012).
- [12] Braun, S. *et al.* Emergence of coherence and the dynamics of quantum phase transitions. *Proc. Natl. Acad. Sci.* **112**, 3641–3646 (2015).
- [13] Fitzsimons, J. F. & Kashefi, E. Unconditionally verifiable blind quantum computation. *Physical Review A* **96**, 012303 (2017).
- [14] Aharonov, D., Ben-Or, M. & Eban, E. Proceedings of innovations in computer science (2010).
- [15] Morimae, T. Verification for measurement-only blind quantum computing. *Physical Review A* **89**, 060302 (2014).
- [16] Hayashi, M. & Morimae, T. Verifiable measurement-only blind quantum computing with stabilizer testing. *Physical review letters* **115**, 220502 (2015).
- [17] Reichardt, B. W., Unger, F. & Vazirani, U. Classical command of quantum systems. *Nature* **496**, 456 (2013).
- [18] McKague, M. Interactive proofs for bqp via self-tested graph states. *Theory of Computing* **12**, 1–42 (2016).
- [19] Fitzsimons, J. F., Hajdušek, M. & Morimae, T. Post hoc verification of quantum computation. *Physical review letters* **120**, 040501 (2018).
- [20] Coladangelo, A., Grilo, A., Jeffery, S. & Vidick, T. Verifier-on-a-leash: new schemes for verifiable delegated quantum computation, with quasilinear resources. *arXiv preprint arXiv:1708.07359* (2017).
- [21] Barz, S., Fitzsimons, J. F., Kashefi, E. & Walther, P. Experimental verification of quantum computation. *Nature physics* **9**, 727 (2013).
- [22] Mahadev, U. Classical verification of quantum computations. In *2018 IEEE 59th Annual Symposium on Foundations of Computer Science (FOCS)*, 259–267 (IEEE, 2018).
- [23] Raussendorf, R. & Briegel, H. J. A one-way quantum computer. *Phys. Rev. Lett.* **86**, 5188 (2001).
- [24] Briegel, H.-J., Browne, D. E., W., D., Raussendorf, R. & Van den Nest, M. Measurement-based quantum computation. *Nat. Phys.* **19**, 5 (2009).
- [25] Fitzsimons, J. F. Private quantum computation: An introduction to blind quantum computing and related protocols. *npj Quantum Information* **3**, 23 (2017).
- [26] IBM Quantum Experience.
- [27] Rigetti Computing.
- [28] Greganti, C. *et al.* Tuning single-photon sources for telecom multi-photon experiments. *Opt. Expr.* **26**, 3286–3302 (2018).
- [29] Mantri, A., Demarie, T. F. & Fitzsimons, J. F. Universality of quantum computation with cluster states and (x, y)-plane measurements. *Sci. Rep.* **7** (2017).
- [30] Danos, V. & Kashefi, E. Determinism in the one-way model. *Phys. Rev. A* **74**, 052310 (2006).
- [31] Browne, D., Kashefi, E., Mhalla, M. & Perdrix, S. Generalized flow and determinism in measurement-based quantum computation. *New J. Phys.* **9**, 250 (2007).
- [32] Mantri, A., Demarie, T. F., Menicucci, N. C. & Fitzsimons, J. F. Flow ambiguity: A path towards classically driven blind quantum computation. *Phys. Rev. X* **7**, 031004 (2017).
- [33] Mhalla, M., Murao, M., Perdrix, S., Someya, M. & Turner, P. S. Which graph states are useful for quantum information processing? In *Conference on Quantum Computation, Communication, and Cryptography*, 174–187 (Springer, 2011).
- [34] Knight, W. & Bloom, D. M. E2386. *Am. Math. Mon.* **80**, 1141–

- 1142 (1973).
- [35] Linke, N. M. *et al.* Experimental comparison of two quantum computing architectures. *Proc Natl. Acad. Sci.* **114**, 3305–3310 (2017).
- [36] Barz, S. *et al.* Demonstration of blind quantum computing. *Science* **335**, 303–308 (2012).
- [37] Lanyon, B. P. *et al.* Measurement-based quantum computation with trapped ions. *Phys. Rev. Lett.* 210501 (2013).
- [38] McCutcheon, W., McMillan, A., Rarity, J. G. & Tame, M. S. Experimental demonstration of a measurement-based realisation of a quantum channel. *New Journal of Physics* **20** (2018).
- [39] Kawamura, M., B. Rowland, B. & Jones, J. A. Preparing pseudopure states with controlled-transfer gates. *Phys. Rev. A* **82**, 032315 (2010).
- [40] Knill, E., Laflamme, R., Martinez, R. & H., T. C. An algorithmic benchmark for quantum information processing. *Nature* **404**, 368 (2000).
- [41] Bowdrey, M. D., Jones, J. A., Knill, E. & Laflamme, R. Compiling gate networks on an ising quantum computer. *Phys. Rev. A* **72**, 032315 (2005).
- [42] Lu, C.-Y. *et al.* Experimental entanglement of six photons in graph states. *Nat. Phys.* **3**, 91–95 (2007).
- [43] Saggio, V. *et al.* Experimental few-copy multi-particle entanglement detection. *arXiv:1809.05455* (2018).
- [44] Broome, M. A., Almeida, M. P., Fedrizzi, A. & White, A. G. Reducing multi-photon rates in pulsed down-conversion by temporal multiplexing. *Opt. Expr.* **19**, 22698–22708 (2011).
- [45] Greganti, C., Roehsner, M. C., Barz, S., Waegel, M. & Walther, P. Practical and efficient experimental characterization of multiqubit stabilizer states. *Phys. Rev. A* **91**, 022325 (2015).
- [46] Dimić, A. & Dakić, B. Single-copy entanglement detection. *npj Quantum Information* **4**, 11–18 (2018).
- [47] 5-qubit backend: IBM Q team, "IBM Q 5 yorktown backend specification V1.0.0," (2017). retrieved from <https://ibm.biz/qiskit-yorktown>.
- [48] Otterbach, J. S. *et al.* Unsupervised machine learning on a hybrid quantum computer. *arXiv:1712.05771* (2017).
- [49] Wendin, G. Quantum information processing with superconducting circuits: a review. *Rep. Prog. Phys.* **80**, 10 (2017).
- [50] Caldwell, S. A. *et al.* Parametrically Activated Entangling Gates Using Transmon Qubits. *Phys. Rev. Appl.* **10**, 034050 (2018).
- [51] Didier, N., Sete, E. A., da Silva, M. P. & Rigetti, C. Analytical modeling of parametrically-modulated transmon qubits. *Phys. Rev. A* **97**, 022330 (2018).
- [52] Sørensen, A. & Molmer, K. Entanglement and quantum computation with ions in thermal motion. *Phys. Rev. A* **62**, 022311 (2000).
- [53] Gottesman, D. & Chuang, I. L. Demonstrating the viability of universal quantum computation using teleportation and single-qubit operations. *Nature* **402**, 390 (1999).
- [54] Gottesman, D. *Stabilizer codes and quantum error correction*. Ph.D. thesis, California Institute of Technology, Pasadena, CA (1997).
- [55] Wang, X.-L. *et al.* Experimental ten-photon entanglement. *Phys. Rev. Lett.* **117** (2016).
- [56] 16-qubit backend: IBM Q team, "IBM Q 16 rueschlikon backend specification V1.0.0," (2017). retrieved from <https://ibm.biz/qiskit-rueschlikon>.

## APPENDIX

**NMR (Oxford)** experiments [7] were performed on a Varian Unity Inova spectrometer with a nominal  $^1\text{H}$  frequency of 600 MHz using a  $\text{H}\{\text{CN}\}$  probe with a single pulsed field gradient. The NMR sample comprised  $^{13}\text{C}$ -labelled sodium formate dissolved in  $\text{D}_2\text{O}$  at 25 °C, providing a heteronuclear two-spin system. With both spins on resonance, the Hamiltonian took the form of a spin–spin  $ZZ$  coupling of 194.7 Hz, and the  $B_1$  field strengths were measured to give nutation rates of approximately 25 kHz for  $^1\text{H}$  and 17 kHz for  $^{13}\text{C}$ .

Pseudo-pure two-qubit states were prepared using the method of Ref. 39. Single-qubit rotations in the  $XY$ -plane were implemented using simple pulses, while two-qubit rotations were implemented as delays. Fixed  $Z$ -rotations were implemented as frame rotations [40] which were propagated through the pulse sequence [41] to points where they could be dropped. The variable small-angle  $Z$ -rotations were implemented using a pair of  $\pi$  pulses with phases separated by  $\theta/2$ , with the phase of the first pulse chosen to partially cancel with the preceding Hadamard gate.

At the end of the algorithm a crush gradient was applied to project the density matrix onto the computational basis, and the  $^1\text{H}$  NMR spectrum observed after a  $\pi/2$  pulse. NMR spectra were processed using custom software and the intensity of the two components of the  $^1\text{H}$  doublet were determined by integration and normalized to a reference spectrum. Corresponding measurements on the second qubit were performed by repeating the experiment with the reverse assignment of qubits to physical spins. From the collection of these measurements the populations of the computational basis states can be estimated. Due to imperfect calibration these populations do not quite sum to one, and some can be slightly negative. This was resolved by subtracting the most negative population found in any group of experiments from all the populations in that group, and then normalizing the populations for each experiment.

**Photons (Vienna)** experiments are based on the generation of the maximally-entangled six-qubit H-shaped cluster state. Three polarization-entangled pairs of photons are produced via three identical Sagnac-PPKTP pulsed down-conversion sources and later entangled by using partial fusion gates at polarizing beam splitters [42, 43]. The qubits are encoded by the polarization of the six photons.

The laser repetition rate is set to 152 MHz, by doubling the original rate with a passive multiplexing scheme [44], to reduce multi-photon noise for an average power of 220 mW per source. The pump photons have a wavelength of 772.9 nm and a pulse-width of 2.1 ps. The crystals' temperature is stabilized at 24 °C. The single-qubit measurements are implemented with an optics tomographic unit of three motorized waveplates and a polarizing beam splitter per photon. Twelve multi-element superconducting-nanowire single-photon detectors, composed of 4 channels each and kept at  $T = 0.9$  K, enable a pseudo-number resolving detection, with

an average quantum efficiency of 0.87. Due to technical problems, two of the multi-element detectors had to be later replaced with two single-element detectors. A customized time tagging and logic module for 48 input-channels counts the six-fold photons events. After postselection we obtain a total six-fold coincidence rate of 0.08 Hz. The purity of the single photons, measured with four-fold HOM interference, corresponds to 0.94 [28]. We characterize the six-photon cluster state by using a subset of stabilizer operators, so-called identity product [45], giving a lower bound on the state fidelity of  $F_{exp} \geq 0.64 \pm 0.04$  and by using a technique based on a probabilistic protocol for entanglement detection [43, 46], estimating a fidelity of  $0.75 \pm 0.06$  (see SM).

**Superconducting (IBM and Rigetti)** qubits are used independently via the two cloud-accessible quantum processors: the *ibmqx2* (also known as *IBM Q 5 Yorktown*) from IBM [26, 47] and the *Rigetti 19Q* from Rigetti [27, 48]. Both apparatuses use *transmon* qubits, charge qubits which show insensitivity to charge noise thanks to an additional large capacitor in the circuit. Variations of the two devices can be found on the circuit wiring and reading, and the fabrication materials, e.g. the *ibmqx2* has a star-shaped connected circuit, based on fixed-frequency transmons [49], with three qubits available as control qubits, whereas the *Rigetti19Q* has tunable-frequency transmon qubits [50, 51], each coupled to three fixed-frequency transmon qubits.

The *ibmqx2* processor was calibrated twice during our experimental runs and kept at a temperature of 17.5 mK. We selected qubits 2, 3, and 4 with frequencies of [5.2, 5.0, 5.3] GHz, single-qubit gate errors of  $[3.4, 3.6, 3.3] \cdot 10^{-3}$ , and readout errors of  $[3.5, 1.5, 1.6] \cdot 10^{-2}$ , respectively. The two-qubit gate errors consist of  $[6.7, 3.7] \cdot 10^{-2}$  for the controlled gate between qubit 2 and 3 and between qubit 2 and 4, respectively. The coherence times are [48.5, 51.7, 39.4]  $\mu$ s for depolarization and [28.9, 75.6, 49.9]  $\mu$ s for spin dephasing, whereas the gate time is  $\sim 250$  ns.

On the *Rigetti19Q* we exploit the qubits labelled 2, 8 and 13, as they show reduced noise. The chip is maintained at a temperature of 10 mK. From [51], single-qubit readout fidelities are equal to 0.97, 0.947, and 0.921, single-qubit gate fidelities correspond to 0.981, 0.987 and 0.993 for qubits 2, 8 and 13, respectively, and two-qubit gate fidelities are 0.906 (between qubit 2 and 8) and 0.881 (between qubit 8 and 13). The qubits coherence time is  $\sim 20$   $\mu$ s, whereas entangling gates time is 100–250 ns.

**Trapped ions (Innsbruck)** experiments are performed with qubits encoded in the electronic states of a string of  $^{40}\text{Ca}^+$  ions confined in a linear Paul trap [8]. Each ion encodes a qubit in the ground state  $S_{1/2}(m = -1/2) = |1\rangle$  and the meta-stable state  $D_{5/2}(m = -1/2) = |0\rangle$ , which determines the qubit lifetime of  $\sim 1$  s. Single qubit Z-rotations are implemented via Stark-shifts induced by tightly focused laser beams, while collective rotations around any equatorial axis of the Bloch-sphere are achieved by resonant illumination of the whole ion string. Entangling operations are implemented via global Mølmer-Sørensen interactions using a bi-chromatic

laser field [52]. Local gates as well as two-qubit entangling gates achieve fidelities greater than 99% and operate on a timescale of 20–30  $\mu$ s (80  $\mu$ s for entangling gates), much faster than the coherence time which is on the order of  $\sim 100$  ms and dominated by laser phase noise. Every run of the experiment consists of Doppler and sideband cooling of the ion string, followed by a gate sequence, and finally projection onto the computational subspace via fluorescence detection on the  $P_{1/2}$ — $S_{1/2}$  transition with a CCD camera. One such run takes  $\sim 15$  ms and each experiment is repeated at least 100 times to gather statistics.

## Supplementary Information: Verification of independent quantum devices

Here we provide full details on the conversion between MBQC and circuit model computations for different choices of flow. We illustrate this using an explicit example from the main text and also provide complementary results on other graph states. Finally, we discuss some additional experimental details of the single-photon implementation.

### CONVERTING BETWEEN CIRCUIT MODEL AND MBQC

The reference gate in MBQC is  $\hat{J}(\alpha) = \hat{H}\hat{R}_z(\alpha)$ , which follows from the basics of the one-qubit teleportation scheme [29, 53]. Single qubit universality is obtained by realizing that  $\hat{J}(\alpha)\hat{J}(0) = \hat{R}_x(\alpha)$ .

The underlying graph for the MBQC pattern can be constructed by decomposing a generic unitary computation on a fixed initial state,  $|+\rangle^{\otimes N}$ , in terms of  $\hat{J}(\alpha)$  gates and  $\hat{C}_Z$  entangling gates. For each  $\hat{J}(\alpha)$  gate we add a vertex, and draw an edge to connect this vertex to the vertex that represents the preceding  $\hat{J}(\alpha)$  gate as dictated by the circuit. This is done recursively, hence creating  $N$  wires, which represent the unitary evolution of each initial qubit state. The last step is drawing an edge for each  $\hat{C}_Z$  gate, by connecting the two vertices representing the  $\hat{J}$  gates that immediately follow the  $\hat{C}_Z$  gate in the quantum circuit representation. These few steps give us the adjacency matrix of a graph  $\mathcal{G} = \{\mathcal{V}, \mathcal{E}\}$ , with vertex set  $\mathcal{V}$ , and edge set  $\mathcal{E}$ . The cardinality of the vertex set is  $|\mathcal{V}| = N + M$ , where  $M$  is the total number of  $\hat{J}(\alpha)$  gates in the circuit.

### CIRCUITS FOR THE 6-QUBIT H-SHAPED CLUSTER

We consider the two quantum circuits shown in Fig. 2 of the main text, associated with the six-qubit H-shaped cluster state. The unitary evolution of two g-flows correspond to:

$$\hat{\mathbf{J}}(\alpha_5, \alpha_6)\hat{\mathbf{J}}(\alpha_3, \alpha_4)C_Z\hat{\mathbf{J}}(\alpha_1, \alpha_2)|++\rangle, \quad (\text{S1})$$

$$\hat{\mathbf{J}}(\alpha_6)\hat{\mathbf{J}}(\alpha_4, \alpha_2)C_{Z_{(1,2)}}\hat{\mathbf{J}}(\alpha_3, \alpha_5)_{1,3}C_{Z_{(1,3)}}\hat{\mathbf{J}}(\alpha_1)|+++\rangle, \quad (\text{S2})$$

where  $\hat{\mathbf{J}}(\alpha_i, \alpha_j) = J(\alpha_i)_1 \otimes J(\alpha_j)_2$  and  $\hat{\mathbf{J}}(\alpha_i, \alpha_j, \alpha_k) = J(\alpha_i)_1 \otimes J(\alpha_j)_2 \otimes J(\alpha_k)_3$ . When using  $\hat{\mathbf{J}}(\alpha_i)$  or  $\hat{\mathbf{J}}(\alpha_i, \alpha_j)$  in a circuit with more qubits, this is implicitly understood as acting on the first set of qubits, unless a subscript indicates which qubits are acted on. The angles  $\alpha$  can be randomly chosen within a specific set. The relationships between correlated outcomes of the circuits  $\mathcal{C}_a$  and  $\mathcal{C}_b$  are

$$\begin{aligned} \Pr(0, 0)_{\mathcal{C}_a} &= 2 \cdot \Pr(0, 0, 0)_{\mathcal{C}_b}, \\ \Pr(0, 1)_{\mathcal{C}_a} &= 2 \cdot \Pr(1, 0, 0)_{\mathcal{C}_b}, \\ \Pr(1, 0)_{\mathcal{C}_a} &= 2 \cdot \Pr(0, 0, 1)_{\mathcal{C}_b}, \\ \Pr(1, 1)_{\mathcal{C}_a} &= 2 \cdot \Pr(1, 0, 1)_{\mathcal{C}_b}, \end{aligned} \quad (\text{S3})$$

where the labels of the outcomes are  $\Pr(b_5, b_6)_{\mathcal{C}_a}$ , and  $\Pr(b_6, b_2, b_5)_{\mathcal{C}_b}$ .

The MBQC protocols can be expressed in terms of the stabilizer formalism [54]. A graph state is invariant under stabilizer operations: Given a graph state on  $n$  qubits  $|\mathcal{G}\rangle = (\prod_{\mathcal{G}} \hat{C}_Z)|+\rangle^{\otimes n}$  we have:

$$\hat{K}_v|\mathcal{G}\rangle = |\mathcal{G}\rangle, \quad \forall v \in \mathcal{V}. \quad (\text{S4})$$

We can rewrite the computation by applying a stabilizer operator on each vertex of the graph state. We consider the stabilizers in their most general form, not restricting to the Pauli group, and a random bit-string  $\mathbf{k} = \{k_i\}_{i=1}^6$ ,  $k_i \in \mathbb{Z}_2$  associated with the six stabilizers. Then the measurement angles  $\alpha$  can be rewritten as

$$\text{angles} = \begin{cases} \tilde{\alpha}_1 = (-1)^{k_1}\alpha_1 + k_3\pi \\ \tilde{\alpha}_2 = (-1)^{k_2}\alpha_2 + (k_4 + r_2)\pi \\ \tilde{\alpha}_3 = (-1)^{k_3}\alpha_3 + (k_1 + k_4 + k_5)\pi \\ \tilde{\alpha}_4 = (-1)^{k_4}\alpha_4 + (k_2 + k_3 + k_6)\pi \\ \tilde{\alpha}_5 = (-1)^{k_5}\alpha_5 + (k_3 + r_3)\pi \\ \tilde{\alpha}_6 = (-1)^{k_6}\alpha_6 + (k_4 + r_1)\pi \end{cases} \quad (\text{S5})$$

where  $\mathbf{r} = \{r_i\}_{i=1}^3$  and can be used to mask the real outcomes of the computation. Note that finding these relations, and thus identifying correlated sampling problems, is computationally efficient because of the graph structure of the problem.

For example, we select the original angle set—randomly generated—to be  $\alpha = \{\frac{3}{4}\pi, \frac{7}{3}\pi, \frac{\pi}{3}, 0, \frac{2}{3}\pi, \pi\}$ , and the random strings to be  $\mathbf{k} = \{1, 0, 0, 0, 1, 0\}$ ,  $\mathbf{r} = \{1, 0, 1\}$ . Using the relations above we get  $\tilde{\alpha} = \{\frac{5}{4}\pi, \frac{7}{3}\pi, \frac{7}{3}\pi, 0, \frac{\pi}{3}, 0\}$ . If we simulate the two circuits we obtain:

$$\Pr(b_5, b_6) = \begin{cases} 0.207 & \text{if } b_5, b_6 = (0, 0), \\ 0.393 & \text{if } b_5, b_6 = (0, 1), \\ 0.043 & \text{if } b_5, b_6 = (1, 0), \\ 0.357 & \text{if } b_5, b_6 = (1, 1), \end{cases} \quad (\text{S6})$$

and

$$\Pr(b_6, b_2, b_5) = \begin{cases} 0.179 & \text{if } b_6, b_2, b_5 = (0, 0, 0), \\ 0.196 & \text{if } b_6, b_2, b_5 = (0, 0, 1), \\ 0.060 & \text{if } b_6, b_2, b_5 = (0, 1, 0), \\ 0.065 & \text{if } b_6, b_2, b_5 = (0, 1, 1), \\ 0.021 & \text{if } b_6, b_2, b_5 = (1, 0, 0), \\ 0.104 & \text{if } b_6, b_2, b_5 = (1, 0, 1), \\ 0.064 & \text{if } b_6, b_2, b_5 = (1, 1, 0), \\ 0.311 & \text{if } b_6, b_2, b_5 = (1, 1, 1). \end{cases} \quad (\text{S7})$$

The strings we have to compare are the following

$$\begin{aligned} \Pr(0,0)c_a &= 2 \cdot \Pr(0 \oplus r_1, 0 \oplus r_2, 0 \oplus r_3)c_b \\ &= 2 \cdot \Pr(1,0,1)c_b, \end{aligned} \quad (\text{S8})$$

$$\begin{aligned} \Pr(0,1)c_a &= 2 \cdot \Pr(1 \oplus r_1, 0 \oplus r_2, 0 \oplus r_3)c_b \\ &= 2 \cdot \Pr(0,0,1)c_b, \end{aligned} \quad (\text{S9})$$

$$\begin{aligned} \Pr(1,0)c_a &= 2 \cdot \Pr(0 \oplus r_1, 0 \oplus r_2, 1 \oplus r_3)c_b \\ &= 2 \cdot \Pr(1,0,0)c_b, \end{aligned} \quad (\text{S10})$$

$$\begin{aligned} \Pr(1,1)c_a &= 2 \cdot \Pr(1 \oplus r_1, 0 \oplus r_2, 1 \oplus r_3)c_b \\ &= 2 \cdot \Pr(0,0,0)c_b. \end{aligned} \quad (\text{S11})$$

By checking the outcomes above, we confirm the correctness of the relations.

### PHOTONIC H-SHAPED CLUSTER STATE CHARACTERIZATION

We first characterize the six-photon cluster state using a technique based on subsets of stabilizer operators, referred to as Identity Products (ID) [45]. The method exploits the entanglement of the operators to obtain a lower bound on the fidelity of the state and a proof of a Bell-type inequality with a minimal number of measurement settings. There exist a large, unquantified number of equivalent minimal subsets of stabilizers for the 6-qubit states. Here we repeat the characterization procedure with two equivalent ID sets, composed of 7 measurements:

ZZIII

ZZIXXX

IIZIYYY

YYXYYYY

YYYYXXX

XXYYYY

YXXXXXX

(a)

ZZIII

ZZIXXX

IIZIYYY

YYXYXX

XXYYYY

XYXXYY

YXXXXY

(b)

where we have omitted the tensor product symbols for compactness. From the ID measurements we extract an ID-Bell parameter  $\langle \alpha_{ID} \rangle_{exp}$ , where  $\alpha_{ID} = \sum_i^M \lambda_i O_i$  and  $M$  is the number of measurements settings in the ID and  $O_i$  is the  $i^{th}$  stabilizer operator of the ID. A Bell-type violation in this case is obtained if  $\langle \alpha_{ID} \rangle_{exp} > M - 2$ . The experimental results show violations of the Bell-type inequality of  $3.4\sigma$  and  $2.4\sigma$ , respectively. A minimum value of the fidelity can be calculated as  $F_{min} = ((\langle \alpha_{ID} \rangle_{exp} - M + 4)/4)$ , providing  $F_{min} = 0.64 \pm 0.04$  for the first ID and  $F_{min} = 0.66 \pm 0.07$  for the second ID. The error bars are reduced for the first set because of a longer acquisition time: 1.5 h and 0.7 h for the first and second set, respectively. The experimental expectation values for the two IDs are reported in Fig. S1. In both cases the results of the 6-qubit H-shaped cluster state show a violation of the ID-Bell inequality and high minimal fidelity. The non-ideal results are mainly due to the unbalanced losses present at the polarizing beam splitters stage, the imperfect

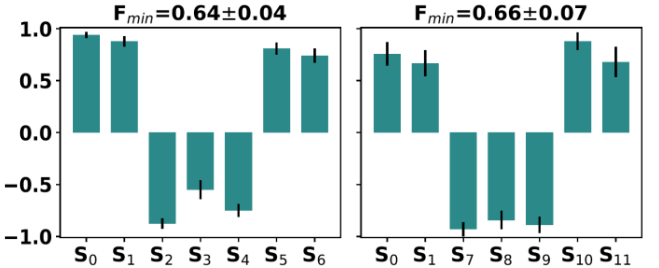


FIG. S1. Expectation values of the measured stabilizer operators for the two identity product related to the 6-qubit H-shaped cluster state.

polarization compensation along the single mode fibers connecting the three sources, and the non-unity purity of the single photons.

Furthermore we follow a probabilistic protocol for entanglement detection [43, 46] in order to estimate the experimental fidelity of the state. This method entails a significant reduction of resources, that is, it needs in our case only a very low number of detection events (around 100) to verify the presence of entanglement in our cluster state with more than 99% confidence. We obtain a fidelity of  $0.75 \pm 0.06$ , which is comparable to fidelities obtained in state-of-the-art photonic experiments [55]. More details about the cluster state characterization can be found in [43].

### COMPLEMENTARY RESULTS

Here we report data related to the evaluation of quantum circuits equivalent to closed lattice cluster states, without performing the respective measurement based quantum computation. Specifically we consider the closed 2D cluster states involving 8 and 10 qubits shown in Fig. S2. We refer to those as Box Cluster 2x4 and Box Cluster 2x5, respectively, with  $2 \times j$  ( $j = [4, 5]$ ) labels the height and width of the cluster.

Different types of circuits are performed on pairs of quantum devices. In the following table all the correlated devices with the implemented circuits specifications (input qubits and circuit depth) are reported.

Box Cluster	input	depth	Q. device
2x4	2	4	Oxford
	2	4	Innsbruck
	4	2	IBM
2x5	2	5	Oxford
	5	2	IBM <sub>2</sub>

Note that the 5x2 cluster was measured using a different IBM device, namely the *ibmqx3* [56] (*IBM Q 16 Rueschlikon*), which we refer to as IBM<sub>2</sub>. This device has similar specifications as the first IBM quantum processor used here, but allows for computations with up to 16 qubits.

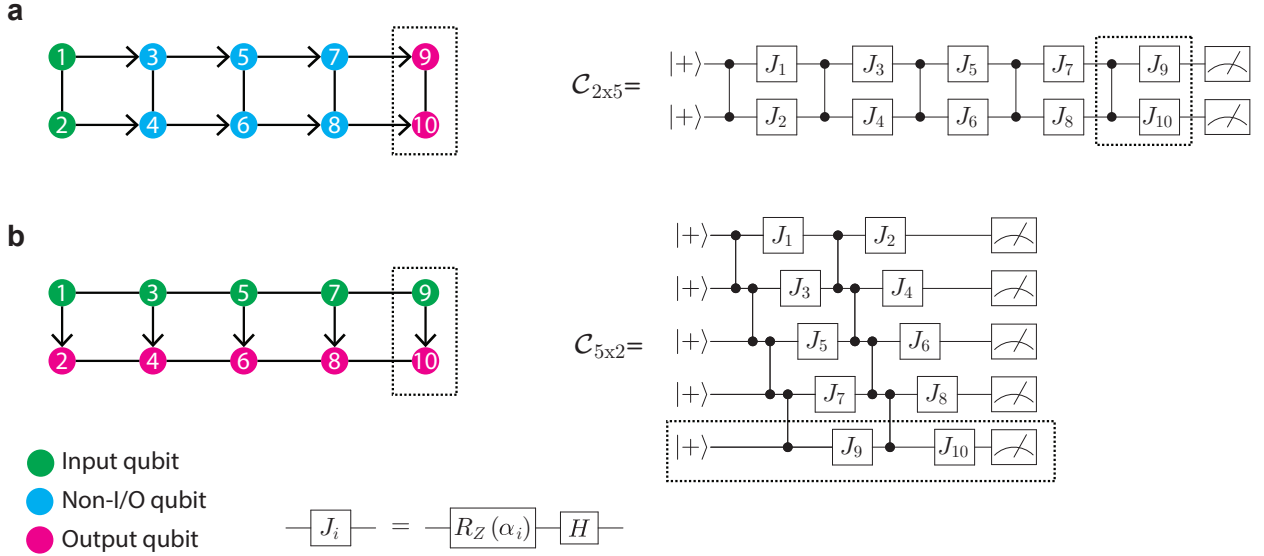


FIG. S2. The Box Cluster 2x5 with two choices of g-flow. **a** The “left-to-right” flow maps to the 2-qubit, depth-5 circuit  $\mathcal{C}_{2x5}$ , whereas the **b** “top-to-bottom” flow maps to a 5-qubit, depth-2 circuit  $\mathcal{C}_{5x2}$ . The construction for the Box Cluster 2x4 is equivalent with the elements in dashed borders removed.

### Box Cluster

As in the main text, the equivalences for the outcome probabilities obtained from the two circuits based on the Box Cluster 2x4 are:

$$\begin{aligned}\Pr(0,0)_{\mathcal{C}_{2x4}} &= 4 \cdot \Pr(0,0,0,0)_{\mathcal{C}_{4x2}}, \\ \Pr(0,1)_{\mathcal{C}_{2x4}} &= 4 \cdot \Pr(0,0,0,1)_{\mathcal{C}_{4x2}}.\end{aligned}$$

Similarly, for the Box Cluster 2x5 we obtain:

$$\Pr(0,0)_{\mathcal{C}_{2x5}} = 8 \cdot \Pr(0,0,0,0,0)_{\mathcal{C}_{5x2}},$$

$$\Pr(0,1)_{\mathcal{C}_{2x5}} = 8 \cdot \Pr(0,0,0,0,1)_{\mathcal{C}_{5x2}}.$$

We ran 100  $\mathcal{C}_{2x4}$  circuits on the Oxford and Innsbruck machines, with the correlated 100  $\mathcal{C}_{4x2}$  circuits run on the IBM processor. For the 2x5 case we ran 100  $\mathcal{C}_{2x5}$  circuits on the Oxford machine and the correlated 100  $\mathcal{C}_{5x2}$  circuits on the IBM processor. In each case, pair-wise cross-check verification was performed between all devices, as well as individual comparisons to theory. Scatterplots of the outcome probabilities are shown in Fig. S3 and all relevant numerical values are given in the caption of that figure. As in the main text, we find that the squared  $\ell_2$  distance enables a very good estimate of the true performance of the devices in agreement with the theory simulation.

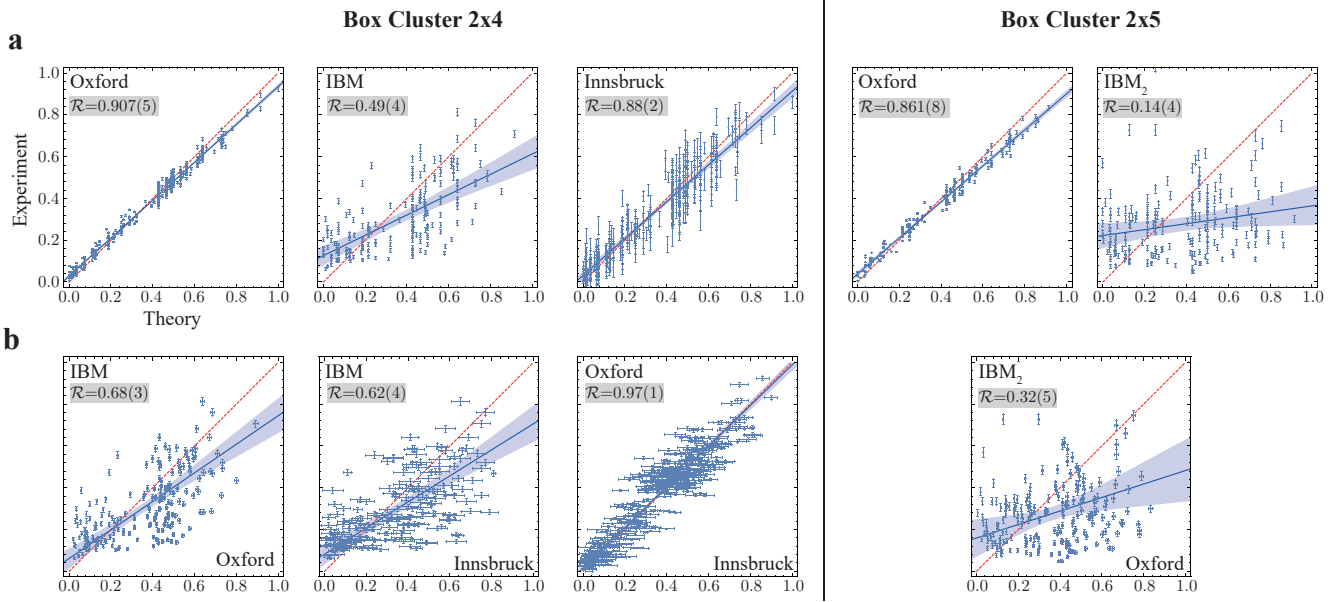


FIG. S3. Data for cross-verification using the Box Cluster 2x4 (left) and 2x5 (right). **(a)** Scatterplots of outcome probabilities compared to the theoretical expectation for (from left to right): Oxford, Innsbruck, IBM for the 2x4-cluster, and Oxford, IBM<sub>2</sub> for the 2x5 cluster. The squared  $\ell_2$ -distances  $\|\mathbf{p}_1 - \mathbf{p}_2\|^2$  for these theory comparisons are 0.00200(3), 0.0578(5), 0.0123(6), 0.00400(8), 0.145(1). This is in good agreement with the trends seen from a linear least-squares regression (blue line) quantifying the deviation from the ideal correlation (red dashed line), with the resulting regression slopes  $\mathcal{R}$  with 1-sigma uncertainties given in the top left corner of the respective figure panel. **(b)** Scatterplots of the outcomes probabilities for two-by-two cross-check verification between Oxford–IBM, Innsbruck–IBM, and Innsbruck–Oxford for the 2x4 cluster, and Oxford–IBM<sub>2</sub> for the 2x5 cluster. The squared  $\ell_2$ -distances  $\|\mathbf{p}_1 - \mathbf{p}_2\|^2$  for the cross-validations are 0.0504(6), 0.060(2), 0.0115(6), 0.118(1). This is in good agreement with the regression coefficients  $\mathcal{R}$  obtained from linear total least squares regression (blue line) given in the top left corner of the respective figure panel. Experimental error bars correspond to 1-sigma statistical uncertainty and the blue shaded bands represent 3-sigma mean prediction intervals for the regression.